

Structural and Photoacoustic Study of Cr₁₁Ge₁₉ Prepared by Mechanical Alloying

Ailton da Silva Ferreira^a, Patricia Bodanese Prates^a, Claudio Michel Poffo^b, João Cardoso de Lima^{c*},
Ronaldo Sergio de Biasi^d

^a Departamento de Engenharia Mecânica, Universidade Federal de Santa Catarina, Campus
Universitário Trindade, S/N, C.P. 476, 88040-900, Florianópolis, SC, Brazil

^b Universidade Federal de Santa Catarina, Campus de Araranguá, 88900-000, Araranguá, SC, Brazil

^c Departamento de Física, Universidade Federal de Santa Catarina, Campus Universitário Trindade,
S/N, C.P. 476, 88040-900, Florianópolis, SC, Brazil

^d Seção de Engenharia Mecânica e de Materiais, Instituto Militar de Engenharia, 22290-270, Rio de
Janeiro, RJ, Brazil

Received: October 22, 2016; Revised: April 21, 2017; Accepted: May 22, 2017

A nanostructured Cr₁₁Ge₁₉ phase was produced by mechanical alloying for 15 h. Decomposition occurred for larger milling times, yielding Cr, Ge, Cr₂O₃ and GeO₂. According to the Cr-Ge phase diagram, the Cr₁₁Ge₁₉ phase is stable up to ≈ 928 °C, but, when submitted to milling, a structural instability causes its decomposition. We studied this structural instability using the coordination numbers and interatomic distances of bulk Cr₁₁Ge₁₉ to simulate the structure factors $S_{CrCr}(K)$, $S_{CrGe}(K)$, and $S_{GeGe}(K)$. The radial distribution functions $RDF_{CrCr}(R)$, $RDF_{CrGe}(R)$ and $RDF_{GeGe}(R)$ were obtained by Fourier transforming the $S_j(K)$ factors, and an important chemical disorder up to ≈ 7 Å was observed in the $RDF_{CrGe}(R)$ and $RDF_{GeGe}(R)$ functions. This chemical disorder was quantified using Cowley-Warren α_{ij}^{CW} parameter. The thermoelectric properties of the Cr₁₁Ge₁₉ phase were also studied.

Keywords: Mechanical alloying; X-ray diffraction; Rietveld method; Photoacoustic absorption spectroscopy; Thermal diffusivity

1. Introduction

Alloys formed by Cr and Ge have potential applications in thermoelectric devices¹ and in the electronic industry²⁻⁴ due to low thermal conductivity and good adherence to silicon substrates. The Cr-Ge phase diagram⁵ has been studied by several researchers⁶⁻¹¹. Liu *et al.*¹⁰ used the CALPHAD method and experimental data to calculate, at room temperature, the enthalpy of formation ΔH for the phases Cr₃Ge ($\Delta H = -15.33$ kJmol⁻¹), Cr₅Ge₃ ($\Delta H = -16.30$ kJmol⁻¹), Cr₁₁Ge₈ ($\Delta H = -16.19$ kJmol⁻¹), CrGe ($\Delta H = -13.85$ kJmol⁻¹), and Cr₁₁Ge₁₉ ($\Delta H = -10.16$ kJmol⁻¹). Zagryazhskii *et al.*¹¹, using the metallographic, X-ray diffraction, and differential thermal techniques investigated the microstructure of Cr_{100-x}Ge_x alloys prepared by fusion. The Cr₅Ge₃ phase was obtained for compositions between $36.0 \leq x \leq 37.5$ at.%; Cr₃Ge for compositions between $37.5 \leq x \leq 38.0$ at.%; Cr₁₁Ge₈ and Cr₁₁Ge₁₉ for compositions between $49.5 \leq x \leq 50.5$ at.%; Cr₁₁Ge₁₉, CrGe and pure Ge for compositions between $63.3 \leq x \leq 70.0$ at.%; Cr₁₁Ge₁₉ and pure Ge for compositions between $75.0 \leq x \leq 80.0$ at.%; and Cr₁₁Ge₁₉ and CrGe for compositions between $60.0 \leq x \leq 62.0$ at.% after annealing. These studies suggest that the formation of microstructures containing more than one phase is related to the small difference between the enthalpies of formation of the Cr-Ge phases.

Mechanical Alloying (MA) is a technique where moderate pressures are applied, and has been used as an alternative way for synthesizing crystalline¹², nanostructured¹³, amorphous¹⁴, and solid solution phases¹⁵. MA has many advantages including processing at low temperatures, easy composition control, use of relatively inexpensive equipment and the possibility of scaling up. It has also been used to produce some commercially important alloys in a much simpler way and, in particular, those alloys whose components present a great difference in their melting points, such as iron and germanium¹⁶, causing difficulties in the use of techniques based on fusion. For some systems, MA provides an increase in the limit of solubility in solid solutions¹². It has been applied to mixtures composed of immiscible elements¹², allowing the formation of unstable solid solutions in equilibrium conditions.

In the last two decades, our research group has been producing materials in the nanostructured, amorphous and solid solution phases using MA. From the structural point of view, nanostructured materials are described by two components: one crystalline, of nanometer dimensions (2-100 nm), which preserves the bulk crystal characteristics, and another interfacial, composed of defect centers (grain boundaries, interphase boundaries, dislocations, etc.). The first one shows strained crystal lattice regions, while the interfacial component has caused controversy in the literature. Gleiter¹⁷ describes it based on a gaseous model, but other authors do not agree

* e-mail: fsc1jcd@fsc.ufsc.br

with this approach¹⁸. The fact that both components have approximately the same number of atoms leads to a strong dependence on the properties of the atomic arrangements on the interfacial component¹⁷. From a technological point of view, manipulation of the interfacial component may offer the possibility of designing new materials with physical properties for specific applications^{17,18}.

Fecht¹⁹ reported results on the thermodynamic properties and the stability of grain boundaries in nanometric metals, which are obtained by inert-gas condensation and compaction or by high-energy cyclic deformation. He showed that there is a critical excess relative volume ($\Delta V/V_0$) for the nanometric structure to remain stable. When $\Delta V/V_0$ is larger than this critical value, the nanometric structure become unstable and decomposition may occur.

More than a decade ago, we proposed a thermodynamic approach to study the formation of binary alloys by MA, starting from blended crystalline elemental metal powders²⁰. In this approach, we assume that the mixture of interfacial components of the elements in the ultrafine composite powder can be treated as an ideal solution, although it is a solid system, and that the solid state reaction in MA begins in this mixture. In order to promote nucleation and growth of new phases, activation energy must be supplied. This energy comes mainly from the mechanical energy of the balls, from elimination of defect centers, and from phase transformation. In order to use the thermodynamic approach to estimate the activation energy necessary to start atomic migration, we assumed the entropy of sublimation of a gas as the cutoff value for the entropy of the ideal solution. This assumption overestimates the entropy of the ideal solution, but that does not change the general conclusions about the formation of alloys by MA. Solutions with calculated activation energies smaller than 0.030 eV/at are expected to yield amorphous alloys, while solutions with larger activation energies form crystalline phases or solid solutions. The thermodynamic approach was based on work by Fecht¹⁹ about the thermodynamic properties and the stability of grain boundaries in nanometric metals, which are obtained by inert-gas condensation and compaction or by high energy cyclic deformation produced in a standard ball mill. The details of the thermodynamic approach are described in Ref. 20 and will not be repeated here.

Recently, the thermodynamic approach was applied to the Cr-Ge system to study the formation of Cr_{100-x}Ge_x alloys by MA. The calculated activation energy (E_a) and excess volume ($\Delta V/V^d$) for different ideal solutions of Cr and Ge at the temperatures 300, 323 and 373 K are listed in Table 1 of Ref. 21 and will not be repeated here. For the phases shown in the Cr-Ge phase diagram⁵, the calculated activation energies at 323 K are: $0.0133 < E_a < 0.0216$ eV for Cr₁₁Ge₁₉; $E_a = 0.0309$ eV for CrGe; $0.0309 < E_a < 0.0409$ eV for Cr₁₁Ge₈; $0.0409 < E_a < 0.0462$ eV for Cr₅Ge₃; and $E_a = 0.0570$ eV for Cr₃Ge. In Ref. 21, a Cr₇₅Ge₂₅ mixture was subjected to MA,

and for milling times up to 15 h a nanostructured Cr₁₁Ge₁₉ phase together with an amorphous phase were formed. For longer milling times, both Cr₁₁Ge₁₉ and amorphous phases decomposed and the Cr₃Ge phase emerged, remaining stable up to the highest milling time (32 h). Although the Cr-Ge phase diagram⁵ shows that the Cr₁₁Ge₁₉ phase is stable up to ≈ 928 °C, decomposition under milling was observed²¹. To the best of our knowledge, this fact has not been reported in the literature. In order to understand the structural instability in the Cr₁₁Ge₁₉ phase promoted by the milling process, a Cr₃₀Ge₇₀ mixture was prepared and subjected to MA. The structural changes for different milling times were investigated by X-ray diffraction (XRD), differential scanning calorimetry (DSC) and photoacoustic absorption spectroscopy (PAS).

2. Experimental Procedure

Binary mixtures of high-purity elemental powders of chromium (Alfa Aesar, purity 99.8%, spherical shape, particle size <10 μm) and germanium (Aldrich, purity 99.999%, spherical shape, particle size <150 μm) with nominal composition of Cr₃₀Ge₇₀ were sealed together with several steel balls 11.0 mm in diameter in a cylindrical steel vial under argon atmosphere. The ball-to-powder weight ratio was 5:1. A Spex Mixer/Mill model 8000 was used to perform MA at room temperature. A ventilation system was used to keep the vial temperature close to room temperature. The XRD pattern of the Cr₃₀Ge₇₀ mixture was recorded before milling ($t = 0$ h). After 5, 10, 15, 20, 30, 40 and 50 h, milling was stopped and the XRD pattern of the powder was recorded using a Philips X-Pert diffractometer equipped with a copper target and a graphite monochromator. After 15 h of milling, the XRD pattern showed an excellent agreement with the Cr₁₁Ge₁₉ and pure Ge phases given in the ICSD codes 43049 and 41980, respectively²². For longer milling times, decomposition of the Cr₁₁Ge₁₉ phase was observed. The XRD patterns were refined using the Rietveld method²³, implemented in the GSAS package²⁴. The XRD pattern of a certified elemental silicon sample was recorded in the same experimental conditions and used to take into account the instrumental broadening for the Rietveld refinements. For each milling time listed above, DSC thermograms were acquired with a heating rate of 10 °C min⁻¹, under nitrogen flow, using a DSC cell model 2010, manufactured by TA Instruments, Inc.

The thermal diffusivity parameter after 15 h of milling was calculated from PAS measurements performed in a homemade device in the open photoacoustic cell (OPC) configuration. The setup consists of a 250 W quartz-tungsten halogen QTH lamp stabilized by a Bentham 605 current power supply. The light beam, after being infrared filtered by a water lens, is mechanically chopped by a Perkin-Elmer light chopper, model 197, and focused onto the sample. The sample is mounted directly onto the front sound inlet of an

Table 1. Structural data for the nanostructured $\text{Cr}_{11}\text{Ge}_{19}$ phase and for the Cr, Ge, Cr_2O_3 and GeO_2 phases for several milling times. Unit cell parameters (a, c), Apparent crystallite size (D), microstrain (ϵ), relative volume fraction (VF).

Milling time (hs)	Phases				
	Ge (111) line	Cr (110) line	$\text{Cr}_{11}\text{Ge}_{19}$ (21 11) line	Cr_2O_3 (110) line	GeO_2 (101) line
5	$a = 5.6681 \text{ \AA}$	$a = 2.8913 \text{ \AA}$			
	D = 25.4 nm	D = 47.1 nm
	$\epsilon = 1.10 \%$	$\epsilon = 0.37 \%$			
	VF = 69.8 %	VF = 30.2 %			
10	$a = 5.6629 \text{ \AA}$	$a = 2.8914 \text{ \AA}$	$a = 5.8180 \text{ \AA}$		
	D = 21.1 nm	D = 33.7 nm	$c = 52.1460 \text{ \AA}$		
	$\epsilon = 1.32 \%$	$\epsilon = 0.52 \%$	D = 40.6 nm
	VF = 63.8 %	VF = 30.7 %	$\epsilon = 0.37 \%$		
					VF = 5.5 %
15	$a = 5.6582 \text{ \AA}$	$a = 2.8785 \text{ \AA}$	$a = 5.8300 \text{ \AA}$		
	D = 19.6 nm	D = 77.6 nm	$c = 52.2043 \text{ \AA}$		
	$\epsilon = 1.41 \%$	$\epsilon = 0.22 \%$	D = 8.2 nm
	VF = 20.7 %	VF = 2.3 %	$\epsilon = 0.0 \%$		
					VF = 77 %
20	$a = 5.6611 \text{ \AA}$	$a = 2.8883 \text{ \AA}$	$a = 5.8172 \text{ \AA}$	$a = 4.9535 \text{ \AA}$	
	D = 6.5 nm	D = 34.7 nm	$c = 52.2154 \text{ \AA}$	$c = 13.6694 \text{ \AA}$	
	$\epsilon = 0.0 \%$	$\epsilon = 0.50 \%$	D = 29.7 nm	D = 23.1 nm	...
	VF = 66.5 %	VF = 8.6 %	$\epsilon = 0.64 \%$	$\epsilon = 0.69 \%$	
					VF = 13.3 %
30	$a = 5.6558 \text{ \AA}$	$a = 2.8836 \text{ \AA}$		$a = 4.9609 \text{ \AA}$	$a = 4.9204 \text{ \AA}$
	D = 20.6 nm	D = 34.7 nm		$c = 13.6012 \text{ \AA}$	$c = 5.5778 \text{ \AA}$
	$\epsilon = 1.35 \%$	$\epsilon = 0.50 \%$...	D = 32.8 nm	D = 39.0 nm
	VF = 68.7 %	VF = 3.0 %		$\epsilon = 0.65 \%$	$\epsilon = 0.74 \%$
					VF = 9.5 %
40	$a = 5.6596 \text{ \AA}$	$a = 2.9027 \text{ \AA}$		$a = 4.9700 \text{ \AA}$	$a = 4.6810 \text{ \AA}$
	D = 15.3 nm	D = 57.0 nm		$c = 13.5710 \text{ \AA}$	$c = 6.1791 \text{ \AA}$
	$\epsilon = 0.87 \%$	$\epsilon = 0.31 \%$...	D = 27.4 nm	D = 20.7 nm
	VF = 57.6 %	VF = 1.6 %		$\epsilon = 0.77 \%$	$\epsilon = 1.27 \%$
					VF = 10.5 %
					VF = 30.2 %

electret microphone²⁵. The output voltage of the microphone is connected to a lock-in amplifier, which in turn is connected to a computer in order to record the PAS signal amplitude and phase as functions of the modulation frequency. The samples for PAS measurements were prepared by pressing the powder at the same pressure to form tiny circular pellets of 10 mm in diameter. The thickness of the as-milled sample was 380 μm . The PAS measurements were taken in the modulation frequency range 10–270 Hz in order to achieve the thermally thick regime.

3. Results and Discussion

3.1 XRD and DSC results

Figure 1 shows the XRD patterns of the $\text{Cr}_{30}\text{Ge}_{70}$ mixture for 0, 5, 10, 15, 20, 30, 40 and 50 h of milling. One can see

that the XRD pattern of blended powders before milling (0 h), besides the diffraction peaks of elemental Cr (* symbol) and Ge (# symbol), shows diffraction peaks of GeO_2 (+ symbol), which are absent in the XRD pattern of elemental Ge powder as received. Probably the nucleation of GeO_2 occurred during manipulation of blended powders to carry out the XRD measurements at ambient conditions, and is probably restricted to the region close to the particle surface. In a previous article²¹, this oxide phase was also observed, but not discussed, in the XRD pattern of blended powders before milling. For a milling time of 5 h, the intensity of the diffraction peaks of pure Ge was smaller than in the initial mixture and the peaks of GeO_2 are absent. Convolution of the (110) Cr and (220) Ge peaks located at about $2\theta \approx 45^\circ$ indicates that a Cr-Ge solid solution phase is forming. For 10 h of milling, besides the peaks observed previously, two low-intensity peaks are seen between $2\theta = 35^\circ$ and $2\theta = 40^\circ$,

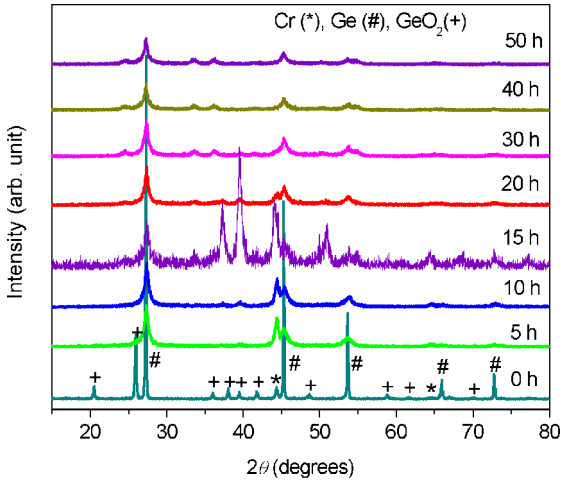


Figure 1. (color online): XRD patterns of a Cr₃₀Ge₇₀ mixture for several milling times.

indicating the formation of one or more new phases. For 15 h of milling, the XRD pattern of the emerging phase(s) is well defined. For 20 h of milling, the previous XRD pattern is still observed, but the intensities of the peaks are much lower. In addition, another XRD pattern similar to that of pure Ge is observed, suggesting a possible decomposition of the majority phase seen at 15 h of milling. For milling times longer than 20 h, besides the diffraction peaks previously observed, peaks located at about $2\theta \approx 24.6^\circ$, 33.8° , and 36° are seen, indicating that a new phase is emerging.

All the XRD patterns shown in Figure 1 were simulated using the Rietveld structural refinement method²³, implemented using the computational GSAS code²⁴, which calculates the relative amount of the phases. A pseudo-Voigt function, $pV(x)$, was used to describe the diffraction peak profiles. All the details about this function as well as its use in Rietveld XRD analysis are presented in Refs. 26-28 and will not be repeated here. For the Rietveld structural refinements, the structural data given in the ICSD codes 64712 for pure Cr, 41980 for pure Ge, 43049 for Cr₁₁Ge₁₉, 25781 for Cr₂O₃, and 16577 for GeO₂ were used. The best fits were obtained for the lattice parameters listed in Table 1. The relative amounts of pure Cr and Ge, Cr₁₁Ge₁₉, Cr₂O₃, and GeO₂ as well as the apparent crystallite size and the microstrain calculated using the single-line method^{26,27} are also listed in Table 1. The apparent crystallite size corresponding to the Cr₁₁Ge₁₉ alloy after 15 h of milling indicates a nanostructured phase.

The Rietveld refinement of the XRD pattern for 5 h of milling (not shown) considering the data for pure Cr and Ge only shows two additional diffraction halos, located at about $2\theta \approx 27^\circ$ and 45° , suggesting the emergence of an amorphous phase. These two halos are better seen in the simulated XRD pattern of Cr. Refinement of the XRD pattern for 10 h of milling (not shown) using data for the previous phases and for Cr₁₁Ge₁₉ yielded a relative volume fraction

of approximately 5.5 % Cr₁₁Ge₁₉. Refinement of the XRD pattern for 15 h of milling using the data for Cr, Ge and Cr₁₁Ge₁₉ (see Figure 2) yielded relative volume fractions of 2.3 % Cr, 20.7 % Ge and 77 % Cr₁₁Ge₁₉. Refinement of the XRD pattern for 20 h of milling considering the previous phases and the data for Cr₂O₃ (not shown) yielded a relative volume fraction of 11.6% Cr₁₁Ge₁₉. Rietveld refinements for the XRD patterns for milling times longer than 20 h (not shown) were performed using only the data for Cr, Ge, Cr₂O₃ and GeO₂. As shown in Table 1, the values of the relative volume fractions of Cr₂O₃ and GeO₂ increase with increasing milling time. Also, it was observed from the refinement of the XRD pattern for 40 h of milling (not shown) that the intensity of two amorphous halos is higher, suggesting that the relative amount of the amorphous phase grows with increasing milling time. As an illustration of the good quality of the refinements, the experimental and simulated XRD patterns for 15 h of milling are shown in Figure 2, where one can see an excellent agreement.

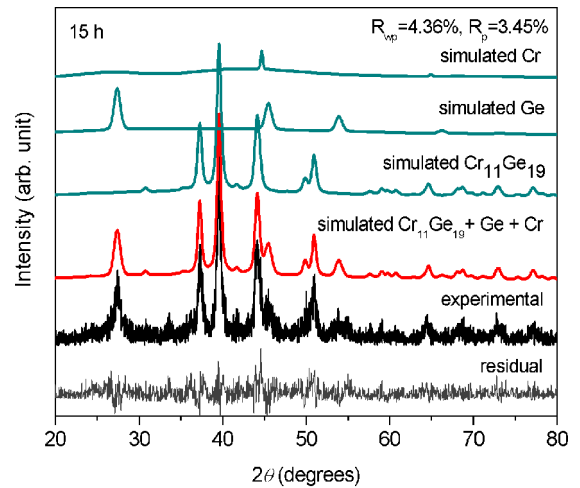


Figure 2. (color online): Experimental and simulated XRD patterns of a Cr₃₀Ge₇₀ mixture milled for 15 h. The difference between experimental and simulated patterns (bottom line) is also shown.

From the results above one can see that for milling times longer than 15 h, the Cr₁₁Ge₁₉ phase starts to decompose into elemental Cr and Ge, but, at the same time, we observe the formation of Cr₂O₃ and GeO₂ phases whose volume fraction increases with increasing milling time. The milling was performed under an argon atmosphere, but the XRD patterns were recorded at ambient conditions. Thus, probably the nucleation and growth of Cr₂O₃ and GeO₂ occurred during manipulation of the as-milled powders to perform the XRD measurements. Probably the oxide phases are restricted to the region close to the particle surface.

The contributions of the nanometric Cr₁₁Ge₁₉ crystallites, interfacial components and the amorphous phase to XRD pattern corresponding to 15 h of milling were estimated using

the procedure described in Ref. 29. The contributions of the interfacial component and the amorphous phase are diffuse and hard to separate. To do this, the measured intensity was corrected for polarization, reabsorption and inelastic scattering and converted to electron units using the mean square scattering factor $\langle f^2(K) \rangle = \sum c_i f_i^2(K)$ ³⁰, where $K=4\pi\sin(\theta)/\lambda$ is the transferred momentum, c_i is the concentration of atoms of type i , $f(K)=f_0(K)+f'(E)+if''(E)$ is the atomic scattering factor, $f'(E)$ and $f''(E)$ are the anomalous dispersion terms, and E is the energy. An evaluation of the background contribution to normalized XRD pattern and its subtraction yields the contribution of nanometric $\text{Cr}_{11}\text{Ge}_{19}$ crystallites. The background was estimated using the OriginLab Corporation software. The ratio between the integrated intensity of the contribution of nanometric $\text{Cr}_{11}\text{Ge}_{19}$ crystallites and the whole XRD pattern gives a crystalline volume fraction of 75.2%, and, consequently, the sum of the interfacial component and amorphous phase corresponds to relative volume fraction of 24.8%. The contributions of pure Cr and Ge were subtracted before calculating the ratio. This procedure is shown in Figure 3. In this figure, the $\langle f^2(K) \rangle$ factor is shown as a function of the diffraction angle 2θ . Rietveld refinement does not take into account the contribution of the background to the relative volume fractions of the phases. Thus, considering the interfacial component and amorphous phase relative volume fraction of 24.8%, the crystalline relative volume fractions of Cr, Ge and $\text{Cr}_{11}\text{Ge}_{19}$ crystallites are 3.1%, 27.5% and 44.6%, respectively.

In order to confirm the nucleation of an amorphous phase, DSC measurements were performed on the sample milled for 15 h; the thermograms are shown in Figure 4. The first measurement (solid red line) shows an exothermic band from 50 to 450 °C and an exothermic peak at 498.17 °C. The exothermic band is attributed to structural relaxation (elimination of defects and atomic diffusive processes) and

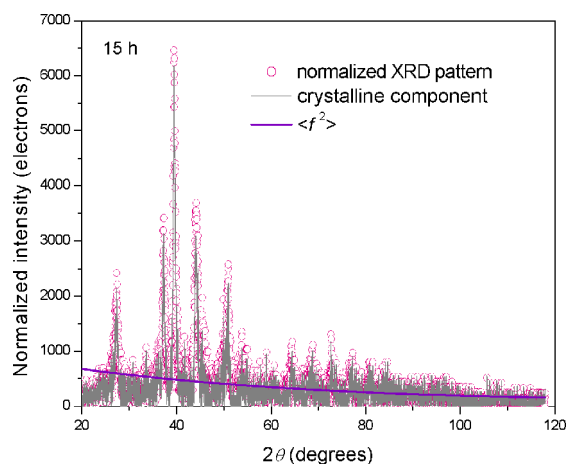


Figure 3. (color online): Normalized XRD pattern of a $\text{Cr}_{30}\text{Ge}_{70}$ mixture milled for 15 h in electron unit: all contributions (open circles line, crystalline contribution (gray line) and the mean square scattering factor $\langle f^2 \rangle$ (violet line).

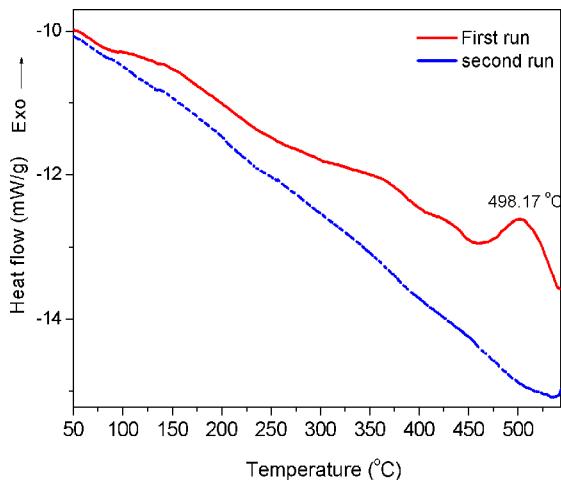


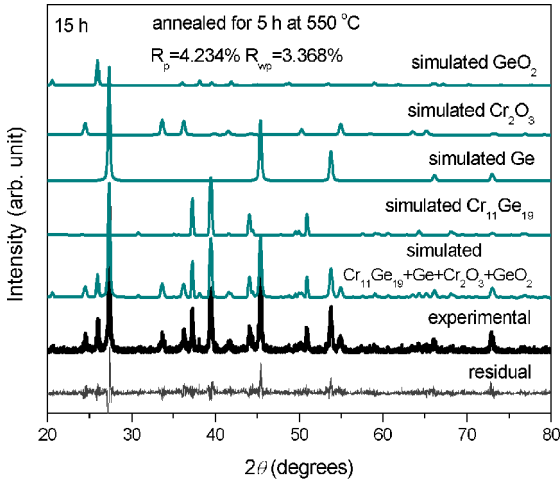
Figure 4. (color online): DSC thermograms of a $\text{Cr}_{30}\text{Ge}_{70}$ mixture milled for 15 h, using a heating rate of 10 °C min^{-1} .

the exothermic peak to crystallization of the amorphous phase. A second thermogram (blue dotted line) was recorded using the same sample in order to confirm the crystallization of the amorphous phase, and the exothermic peak seen previously is absent.

In order to investigate the structural stability of the $\text{Cr}_{11}\text{Ge}_{19}$ phase upon heating, two batches of a sample milled for 15 h were sealed in tubes of quartz evacuated to a pressure of less than 10^{-3} Torr, annealed at 550 °C for different periods of time, 30 min and 5 h, and cooled in air. The XRD patterns of the annealed samples were recorded and refined by the Rietveld method^{23,24}. The XRD pattern for 30 min of annealing was refined using the ICSD codes for Ge, $\text{Cr}_{11}\text{Ge}_{19}$, and Cr_2O_3 , whereas that for 5 h of annealing was refined using the same ICSD codes plus that for GeO_2 . The best fits were obtained for the lattice parameters listed in Table 2. This table also shows the relative volume fractions for Ge, $\text{Cr}_{11}\text{Ge}_{19}$, Cr_2O_3 , GeO_2 , the apparent crystallite size (D), and microstrain (ϵ) determined using the single-line method²⁶⁻²⁸. Figure 5 shows the experimental and simulated XRD patterns for the sample annealed for 5 h. In order to understand the sequence of formation of the Cr_2O_3 and GeO_2 phases with increasing annealing time, an analysis of the enthalpies of formation may be helpful. According to the TAPP software⁵, the enthalpies of formation for the Cr_2O_3 and GeO_2 phases are $-1058.11\text{ kJmol}^{-1}$ and $-521.30\text{ kJmol}^{-1}$, respectively. These values show that the Cr_2O_3 phase is nucleated before the GeO_2 phase. The Table 2 shows that the relative volume fraction for the $\text{Cr}_{11}\text{Ge}_{19}$ phase is smaller for 5 h of annealing than for 30 min. This result suggests its decomposition progressively into pure Cr and Ge upon annealing. Under milling, its complete decomposition into pure Cr and Ge seems to be faster. Again, the observed oxidation is attributed to the manipulation of annealed samples for the XRD measurements at ambient conditions.

Table 2. Structural data for the nanostructured Cr₁₁Ge₁₉ phase and for the Cr, Ge, Cr₂O₃ and GeO₂ phases after 15 h of milling and annealed for 30 and 300 min at 550 °C. Unit cell parameters (*a*, *c*), Apparent crystallite size (*D*), microstrain (ϵ), relative volume fraction (VF).

Annealing Time (min)	Phases				
	Ge (111) line	Cr (110) line	Cr ₁₁ Ge ₁₉ (21 11) line	Cr ₂ O ₃ (110) line	GeO ₂ (101) line
30	<i>a</i> = 5.6540 Å		<i>a</i> = 5.8086 Å	<i>a</i> = 4.9584 Å	
	<i>D</i> = 55.1 nm		<i>c</i> = 52.3834 Å	<i>c</i> = 13.5868 Å	
	ϵ = 0.43 %	...	<i>D</i> = 31.2 nm	<i>D</i> = 44.3 nm	...
	VF = 42.4 %		ϵ = 0.10 %	ϵ = 0.48 %	
300	<i>a</i> = 5.6492 Å		<i>a</i> = 5.8025 Å	<i>a</i> = 4.9573 Å	<i>a</i> = 4.9793 Å
	<i>D</i> = 70.5 nm		<i>c</i> = 52.3457 Å	<i>c</i> = 13.5657 Å	<i>c</i> = 5.6382 Å
	ϵ = 0.40 %	...	<i>D</i> = 51.2 nm	<i>D</i> = 31.8 nm	<i>D</i> = 77.4 nm
	VF = 36.1 %		ϵ = 0.15 %	ϵ = 0.67 %	ϵ = 0.38 %
			VF = 31.7 %	VF = 24.2 %	VF = 8.0 %

**Figure 5.** (color online): Experimental and simulated XRD patterns of a Cr₃₀Ge₇₀ mixture milled for 15 h and annealed for 5 h at 550 °C. The difference between experimental and simulated patterns (bottom line) is also shown.

The oxide phases are probably restricted to the region close to the particle surface.

Chemical disorder is among the physical mechanisms responsible for phase transition, amorphization and decomposition of alloys under pressure and/or temperature, but it has not received the attention it deserves. In this study, we investigate the influence of this mechanism on decomposition of the nanostructured Cr₁₁Ge₁₉ phase under milling. The Cowley-Warren chemical short-range order (CSRO) parameter used to study the statistical distribution of atoms in solids, is given by³¹

$$\alpha_{ij}^{CW} = 1.0 - \frac{N_{ij}}{c_j [c_j (N_{ii} + N_{ij}) + c_i (N_{jj} + N_{ji})]}, \quad (1)$$

where N_{ii} , N_{ij} and N_{jj} are the coordination numbers and c_i and c_j are the concentrations of atoms of the elements *i* and *j*.

The α^{CW} parameter is zero for a random distribution, negative if there is a preference for forming unlike pairs and positive if homopolar pairs (clusters or local order) are preferred. Although the α^{CW} parameter is usually applied to amorphous phases, it can also be used to determine the relative preference for forming different atomic pairs and thus to investigate the crystallization behavior of a binary alloy. In order to obtain the coordination numbers N_{CrCr} , N_{CrGe} , N_{GeCr} and N_{GeGe} , the structural data given in ICSD 43049 for the Cr₁₁Ge₁₉ phase were used in the Crystal Office 98 software³² to build the 3D structure, and using the tool “shell structure” the R_{CrCr} , R_{CrGe} and R_{GeGe} interatomic distances were calculated up to 10 Å. The ICSD code 43049 gives the following data: tetragonal structure (S.G. P-4 n 2, No. 118, Z=4, *a* = *b* = 5.8 Å, *c* = 52.34 Å, $\alpha = \beta = \gamma = 90^\circ$), twelve Cr atoms at the Wyckoff positions Cr1 2a (0, 0, 0), Cr2 2c (0, 0.5, 0.25), Cr3 4e (0, 0, 0.0909), Cr4 4e (0, 0, 0.1818), Cr5 4e (0, 0, 0.2723), Cr6 4e (0, 0, 0.364), Cr7 4e (0, 0, 0.4543), Cr8 4h (0, 0.5, 0.0684), Cr9 4h (0, 0.5, 0.1589), Cr10 4h (0, 0.5, 0.5227), Cr11 4h (0, 0.5, 0.6131), Cr12 4h (0, 0.5, 0.7047), and ten Ge atoms at the Wyckoff positions Ge1 4g (0.679, 0.179, 0.25), Ge2 8i (0.239, 0.348, 0.0132), Ge3 8i (0.843, 0.208, 0.04), Ge4 8i (0.313, 0.167, 0.066), Ge5 8i (0.677, 0.327, 0.0922), Ge6 8i (0.159, 0.298, 0.1184), Ge7 8i (0.778, 0.153, 0.1442), Ge8 8i (0.348, 0.258, 0.1712), Ge9 8i (0.783, 0.342, 0.1976), Ge10 8i (0.163, 0.196, 0.224). By putting Cr and Ge atoms at origin, twelve Cr-Cr and Cr-Ge shell structures and ten Ge-Ge and Ge-Cr shell structures were obtained. Of course, the number of repetitions of a specific R_p interatomic distance corresponding to a specific *ij* atomic pair is equal to the coordination number N_{ij} at this distance. All the shell structures showed very close interatomic distances, making difficult to identify the lower and upper limits of the coordination shells. Then, the N_{ij} and R_p values were used to calculate the $S_{CrCr}(K)$, $S_{CrGe}(K)$ and $S_{GeGe}(K)$ structure factors using the expression³³

$$S_{ij}(K) = 1 + \sum_p N_p \sum_{i=K_{min}}^{K_{max}} \frac{\sin(R_p K_i)}{R_p K_i} \quad (2)$$

where K is the transferred momentum. The $0.05 \text{ \AA}^{-1} \leq K \leq 12 \text{ \AA}^{-1}$ interval, with step $\Delta K = 0.05 \text{ \AA}^{-1}$, was used.

The partial reduced distribution functions $\gamma_{ij}(R)$ are related to $S_{ij}(K)$ by Fourier transformation and may be written as

$$\gamma_{ij}(R) = 4\pi\rho_0 R [G_{ij}(R) - 1] = (2/\pi) \int_0^\infty K [S_{ij}(K) - 1] \sin(KR) dK. \quad (3)$$

The partial radial distribution functions $RDF_{ij}(R)$ may be written as

$$RDF_{ij}(R) = 4\pi\rho_0 c_j R^2 G_{ij}(R), \quad (4)$$

where ρ_0 is the atomic density of the alloy in \AA^{-3} and c_j is the concentration. The average interatomic distances R_{ij} of the coordination shells are obtained from the maxima of $\gamma_{ij}(R)$, whereas the coordination numbers N_{ij} are obtained by integrating the peaks of $RDF_{ij}(R)$.

Figure 6a-c shows the calculated $RDF_{CrCr}(R)$, $RDF_{CrGe}(R)$, and $RDF_{GeGe}(R)$ functions (solid lines) using the Cr-Cr, Cr-Ge, and Ge-Ge distances given by the Crystal Office 98 software. In this figure, the symbols are the interatomic distances and coordination numbers (number of repetitions of these distances) given by the Crystal Office 98 software. All the calculated γ_{CrCr} and $RDF_{CrCr}(R)$ functions are similar to those shown in Figure 6a. From the $RDF_{CrGe}(R)$ and $RDF_{GeGe}(R)$ functions shown in Figures 6b and 6c one can see an important chemical disorder in the Cr-Ge and Ge-Ge pairs up to $R \approx 7 \text{ \AA}$. The γ_{CrGe} and γ_{GeGe} functions are not shown. These results show that Eq. (2)

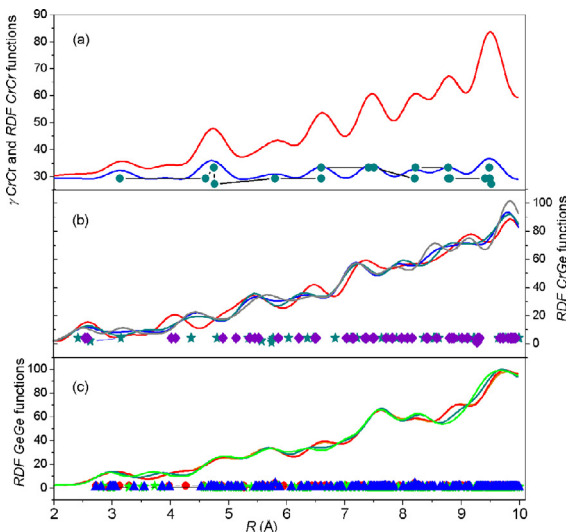


Figure 6. (color online): Partial reduced distribution and radial distribution functions simulated using the interatomic distances up to 10 \AA given by the Crystal Office 98 software in Eq. (2). The symbols are the interatomic distances and coordination numbers obtained by using the Crystal Office 98 software (see text): γ_{CrCr} (blue line) and RDF_{CrCr} (red line) (a); $RDF_{CrGe}(R)$ (colored lines) (b); and $RDF_{GeGe}(R)$ (colored lines) (c).

is a good approach to simulate the $S_{ij}(K)$ factors. Using the lower and upper limits of the first three coordination shells, the coordination numbers were obtained. The values are similar to those obtained from the Crystal Office 98 software. By considering the twelve $RDF_{CrCr}(R)$ and $RDF_{CrGe}(R)$ functions, the average coordination number and interatomic distance values of first three coordination shells are $N_{CrCr} = 4$ at $\approx 3.12 \text{ \AA}$, $N_{CrCr} = 14$ at $\approx 4.73 \text{ \AA}$, $N_{CrCr} = 4$ at $\approx 5.79 \text{ \AA}$, $N_{CrGe} = 8$ at $\approx 2.58 \text{ \AA}$, $N_{CrGe} = 10$ at $\approx 3.31 \text{ \AA}$, and $N_{CrGe} = 22$ at $\approx 4.26 \text{ \AA}$, whereas considering the ten $RDF_{GeGe}(R)$ functions the values are $N_{GeGe} = 8$ at $\approx 3.0 \text{ \AA}$, $N_{GeGe} = 4$ at $\approx 3.96 \text{ \AA}$, and $N_{GeGe} = 15$ at $\approx 4.94 \text{ \AA}$. The coordination numbers for the N_{GeCr} neighbors are obtained using the relationship $c_{Cr} N_{CrGe} = c_{Ge} N_{GeCr}$. Using the values above in Eq. (1), values of $\alpha_{CrGe}^{CW} = -0.04$, $\alpha_{CrGe}^{CW} = 0.15$, and $\alpha_{CrGe}^{CW} = -0.31$ are obtained for the 1st, 2nd and 3rd coordination shells, respectively. These values indicate a random distribution of Cr and Ge atoms in the first shell, a preference for forming homopolar pairs in the second shell and a preference for forming unlike pairs in the third shell. The calculated α^{CW} values for the 1st and 2nd coordination shells suggest that the repulsive part of the crystalline field plays an important role in the structural stability of this phase.

According to Fecht¹⁹, there is a critical excess volume ($\Delta V/V_0$) for which the nanometric structure remains stable. When $\Delta V/V_0$ is larger than this critical excess volume, the nanometric structure become unstable and decomposition may occur. For nanometric pure Cr and Ge powders, the critical excess volumes are $\Delta V/V_0 = 0.392$ and 0.428 , respectively. As shown in Ref. 21, an ideal solution with $\text{Cr}_{11}\text{Ge}_{19}$ nominal composition has $\Delta V/V_0 = 0.415$. For 15 h of milling, the interfacial and amorphous volume fractions of the nanostructured $\text{Cr}_{11}\text{Ge}_{19}$ alloy occupy an excess volume $\Delta V/V_0 = 0.248$. Figure 1 shows that for milling times longer than 20 h the nanostructured $\text{Cr}_{11}\text{Ge}_{19}$ alloy is gradually disappearing and it is no more seen at 30 h of milling. This indicates that the excess volume $\Delta V/V_0$ is increasing with increasing milling time, and increasing also the structural instability of $\text{Cr}_{11}\text{Ge}_{19}$. We believe that the chemical disorder present in the first and second Cr-Ge and Ge-Ge coordination shells increases with increasing excess volume $\Delta V/V_0$, and probably promotes decomposition of the nanostructured $\text{Cr}_{11}\text{Ge}_{19}$ phase when $\Delta V/V_0 > 0.415$.

3.2. PAS measurements

The use of photoacoustic absorption spectroscopy to determine the thermal diffusivity parameter and/or the transport properties of semiconducting materials is widely documented in the literature³⁴⁻⁴⁰ and references therein. The thermal diffusivity may be calculated using the expression for the thermal conductivity $K_t = \rho C_p \alpha$, where ρ is the density, C_p is the specific heat, and α is the thermal diffusivity. For the $\text{Cr}_{11}\text{Ge}_{19}$ phase, the TAPP software⁵ gives values of $\rho = 7359 \text{ kg m}^{-3}$ and $C_p = 359 \text{ J kg}^{-1} \text{ K}^{-1}$. Caillat *et al.*⁴¹

reported a value $K_t = 4.1 \text{ W m}^{-1}\text{K}^{-1}$ at room temperature for the Cr₁₁Ge₁₉ phase. Using these values in expression for the thermal conductivity above, a value of $\alpha = 1.552 \times 10^{-6} \text{ m}^2\text{s}^{-1}$ or $0.01552 \text{ cm}^2\text{s}^{-1}$ is obtained. Those researchers also reported a value of electrical resistivity at room temperature of $\rho_e = 1.7 \mu\Omega \text{ m}$. The electrical conductivity $\sigma_e = 1/\rho_e = 0.5882 \times 10^6 \Omega^{-1}\text{m}^{-1}$ shows that this phase has a character of conductive material ($\sigma_e > 10^5 \Omega^{-1}\text{m}^{-1}$ and no band gap ($E_g = 0$). The characteristic frequency $f_c = \alpha/(\pi l_s^2)$, where l_s is the sample thickness, f_c is the modulation frequency corresponding to the transition from the thermally thin regime ($f < f_c$) to the thermally thick regime ($f > f_c$). The as-milled sample thickness was $380 \mu\text{m}$, giving a characteristic frequency of 3.4 Hz . In order to perform PAS measurements in the thermally thick regime, the data were acquired between 10 and 270 Hz.

The recorded PAS signal amplitude and phase for the as-milled Cr₁₁Ge₁₉ phase after 15 h of milling are shown in the inset of Figure 7. One can see that both amplitude and phase decrease with increasing modulation frequency. Due to the high thermal conductance of the Cr₁₁Ge₁₉ phase, only the intraband nonradiative thermalization (thermal diffusion) and/or thermoelastic bending mechanisms contribute to PAS signal. Thermal diffusion occurs in the low frequency range, followed by thermoelastic bending. The procedure to find the contribution of each process to pressure variation in the photoacoustic cell is described in Ref. 40 and it will not be repeated here. Figure 7 shows the plots $\ln(S)$ vs \sqrt{f} and Φ_{ph} (rad) vs \sqrt{f} for modulations frequencies between 22 and 32 Hz, where the thermal diffusion mechanism is the main contribution to PAS signal amplitude and phase. In this frequency range, the slopes of the straight lines are $a = -0.3108$ (for the amplitude) and $a = -0.3082$ (for the phase). Using the expression $\alpha = \pi(l_s^2/a)$, the values of $\alpha_{eff} =$

$0.047 \text{ cm}^2\text{s}^{-1}$ for the amplitude and $\alpha_{eff} = 0.048 \text{ cm}^2\text{s}^{-1}$ for the phase are calculated.

As shown in Figure 2, the microstructure of the as-milled sample for 15 h is formed by the Cr, Ge and Cr₁₁Ge₁₉ phases. The effective thermal diffusivity α_{eff} is described by the Lichtenecker's logarithmic mixture law^{42,43},

$$\alpha_{eff} = \prod_{n=1}^3 \alpha_n^{x_n} \quad (5)$$

where n is the number of phases; x and α are the volume fraction and thermal diffusivity of each phase, respectively. Using the data for Cr and Ge given in the software PTOE⁴⁴ in the expression for the thermal conductivity $K_t = \rho C_p \alpha$, thermal diffusivity values of $\alpha_{Cr} = 0.2896 \text{ cm}^2\text{s}^{-1}$ for Cr and $\alpha_{Ge} = 0.3517 \text{ cm}^2\text{s}^{-1}$ for Ge are obtained. Using an average thermal diffusivity value of $\langle \alpha_{eff} \rangle = 0.0475 \text{ cm}^2\text{s}^{-1}$ for the as-milled sample for 15 h and the relative volume fraction values of Cr (3.1 %), Ge (27.5 %) and Cr₁₁Ge₁₉ (69.4 %) [crystalline (44.6 %) + interfacial plus amorphous (24.8 %) components] in expression (5), a value of $\alpha = 0.01978 \text{ cm}^2\text{s}^{-1}$ is obtained for the nanostructured Cr₁₁Ge₁₉ phase plus an amorphous phase. This value is slightly larger than that calculated using data from the Refs. 5 and 41 ($\alpha = 0.01552 \text{ cm}^2\text{s}^{-1}$). The difference is attributed to the nanometric structure of the Cr₁₁Ge₁₉ phase and the presence of an amorphous phase.

The performance of a thermoelectric material can be improved if its thermal conductivity is reduced without a significant degradation of its electrical properties. It has been reported that materials having small crystallite size have larger thermoelectric conversion efficiency due a decrease in thermal conductivity⁴⁵. Thermoelectric materials are characterized by a dimensionless figure of merit, $ZT = (S^2 \sigma_e K_t^{-1} T)$, where S is the Seebeck coefficient, σ_e is the electrical conductivity, K_t is the thermal conductivity, and T is the absolute temperature. For high performance, a thermoelectric material should have $ZT > 1$. As shown in Table 1, the apparent crystallite size for the Cr₁₁Ge₁₉ phase after 15 h of milling has nanometer dimensions ($D = 8.2 \text{ nm}$). It is interesting to estimate the influence of the apparent crystallite size on ZT . The thermal conductivity K_t may be estimated using the previously given expression and a specific heat $C_p = 359 \text{ J kg}^{-1} \text{ K}^{-1}$. From the Rietveld refinement of the XRD pattern for 15 h of milling, a density value of $\rho = 7302 \text{ kg m}^{-3}$ was obtained. Considering the thermal diffusivity value of $\alpha = 0.01978 \times 10^{-4} \text{ m}^2 \text{ s}^{-1}$, a value of $K_t = 5.2 \text{ W m}^{-1}\text{K}^{-1}$ was obtained. This value is slightly larger than that reported in Ref. 41. For the Cr₁₁Ge₁₉ phase, this reference reports a value of $S \approx 34 \mu\text{V/K}$ for the Seebeck coefficient. Using these values in the expression for ZT , a value of $ZT \approx 0.0393$ at room temperature is obtained. This value is slightly smaller than that calculated using the data given in Ref. 41 ($ZT \approx 0.0497$). Of course, for an accurate evaluation of ZT , the parameters σ_e , C_p , and S for the nanostructured Cr₁₁Ge₁₉ phase should be measured.

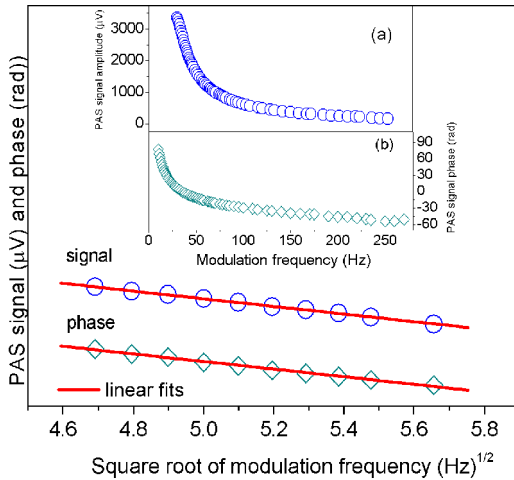


Figure 7. (color online): PAS amplitude (upper line) and PAS phase (lower line) vs modulation frequency of a Cr₃₀Ge₇₀ mixture milled for 15 h showing the intraband nonradiative thermalization (thermal diffusion) mechanism. Inset: (a) PAS amplitude and (b) PAS phase vs modulation frequency.

4. Conclusions

In this work, a nanostructured $\text{Cr}_{11}\text{Ge}_{19}$ phase was successfully produced by mechanical alloying and its structural stability under milling was investigated. A thermodynamic analysis suggested that other Cr-poor alloys could be formed and, in fact, an amorphous phase was also formed. For milling times longer than 15 h, decomposition of the $\text{Cr}_{11}\text{Ge}_{19}$ phase into pure Cr and Ge was observed. Due to the presence of oxygen within the milling vial and/or during manipulation of the as-milled samples to perform XRD measurements at ambient conditions, nucleation and growth of Cr_2O_3 and GeO_2 occurred. These oxide phases are probably restricted to the region close to the particle surface. Using the Cr-Cr, Cr-Ge and Ge-Ge interatomic distances and coordination numbers up to 10 Å obtained by using the Crystal Office 98 software, the $S_{\text{CrCr}}(K)$, $S_{\text{CrGe}}(K)$ and $S_{\text{GeGe}}(K)$ structure factors were simulated, and their Fourier transformation permitted to obtain the $RDF_{\text{CrCr}}(R)$, $RDF_{\text{CrGe}}(R)$ and $RDF_{\text{GeGe}}(R)$ radial distribution functions. The $RDF_{\text{CrGe}}(R)$ and $RDF_{\text{GeGe}}(R)$ functions showed an important chemical disorder up to ≈ 7 Å, suggesting that the decomposition of the $\text{Cr}_{11}\text{Ge}_{19}$ phase into pure Cr and Ge may be related with this strong chemical disorder, which increases with increasing milling time. The calculated Cowley-Warren chemical short-range order (CSRO) parameter values for the first three coordination shells indicated a random distribution of Cr and Ge atoms in the first shell, a preference for forming homopolar pairs in the second shell, and a preference for forming unlike pairs in the third shell.

The PAS analysis yielded a value of $\alpha = 0.01978 \text{ cm}^2 \text{ s}^{-1}$ for the thermal diffusivity parameter of the nanostructured $\text{Cr}_{11}\text{Ge}_{19}$ phase plus an amorphous phase. This value is slightly larger than that calculated for the bulk $\text{Cr}_{11}\text{Ge}_{19}$ phase ($\alpha = 0.01552 \text{ cm}^2 \text{ s}^{-1}$) using data from the literature. The calculated dimensionless figure of merit ZT for the thermoelectric nanostructured $\text{Cr}_{11}\text{Ge}_{19}$ phase ($ZT \approx 0.0393$) is slightly smaller than that reported in the literature for the bulk $\text{Cr}_{11}\text{Ge}_{19}$ phase ($ZT \approx 0.0497$).

5. Acknowledgments

The author Ailton da Silva Ferreira thanks CNPq for financial support.

6. References

- Pécheur P, Toussaint G, Kenzari H, Malaman B, Welter R. Ferromagnetism of the chimney-ladder compound $\text{Cr}_{11}\text{Ge}_{19}$. *Journal of Alloys and Compounds*. 1997;262-263:363-365.
- Borek MA, Oktyabrsky S, Aboelfotoh MO, Narayan J. Low resistivity copper germanide on (100) Si for contacts and interconnections. *Applied Physics Letters*. 1996;69(23):3560.
- Agnelo PD, Kesan VP, Tejwani M, Ott JA. Titanium silicide/germanide formation on submicron features for high mobility SiGe channel field effect transistors. *Journal of Electronic Materials*. 1994;23(4):413-421.
- Ashburn SP, Öztürk MC, Wortman JJ, Harris G, Honeycutt J, Maher DM. Formation of titanium and cobalt germanides on Si (100) using rapid thermal processing. *Journal of Electronic Materials*. 1992;21(1):81-86.
- TAPP Software, Version 2.2. E.S. Wade Court: Microwave Inc.; 1998.
- Yassin A, Castanet R. Calorimetric study of Cr-Ge alloys. *Intermetallics*. 1999;7(1):79-82.
- Jandl I, Richter KW. A revision of the central part of the Cr-Ge phase diagram. *Journal of Alloys and Compounds*. 2010;500(1):L6-L8.
- Zaremba SN, Myers CE, Kematich RJ, Zavalij PY, Whittingham MS, Cotts EJ. Vaporization thermodynamics and heat capacities of Cr_3Ge and Cr_5Ge_3 . *Journal of Alloys and Compounds*. 2001;329(1-2):97-107.
- Goswami R, Kioseoglou G, Hanbicki AT, Jonker BT, Spanos G. Formation of Cr-germanide nanoparticles during growth of epitaxial Ge-Cr thin films. *Acta Materialia*. 2004;52(8):2419-2427.
- Liu YQ, Du Y. Thermodynamic description of the Cr-Ge system. *Calphad*. 2010;34(1):26-35.
- Zagryazhskii VL, Shtol'ts AK, Gel'd PV, Kuz'menko NV. Phase diagram of the system chromium-germanium. *Soviet Powder Metallurgy and Metal Ceramics*. 1966;5(8):639-642.
- Suryanarayana C. Mechanical alloying and milling. *Progress in Materials Science*. 2001;46(1-2):1-184.
- de Lima JC, Borba EC, Paduani C, dos Santos VHF, Grandi TA, Rechenberg HR, et al. Mechanical alloying of Fe and Zn: phase analysis and Mössbauer studies. *Journal of Alloys and Compounds*. 1996;234(1):43-47.
- de Lima JC, Jerônimo AR, Gomez A, Souza SM, Trichês DM, Campos CEM, et al. Structural investigation of an amorphous $\text{Si}_{24}\text{Nb}_{76}$ alloy produced by mechanical alloying using reverse Monte Carlo simulations. *Journal of Non-Crystalline Solids*. 2008;354(40-41):4598-4602.
- Peña Rodríguez VA, Baggio-Saitovitch EM, Xia SK, Larica C, de Lima JC. Mechanical alloying of Fe and Cr: Structural and magnetic studies. *Hyperfine Interactions*. 1992;69(1):721-724.
- de Lima JC, Silva JER, Grandi TA, Sartorelli ML, Silva MR, Filho AB, et al. X-Ray Diffraction, Mössbauer and Magnetization Studies of Nanocrystalline $\text{Fe}_{33}\text{Ge}_{67}$ Alloy Prepared by Mechanical Alloying. *Hyperfine Interactions*. 2001;136(1):45-56.
- Gleiter H. Materials with ultrafine microstructures: Retrospectives and perspectives. *Nanostructured Materials*. 1992;1(1):1-19.
- Stern EA, Siegel RW, Newville M, Sanders PG, Haskel D. Are Nanophase Grain Boundaries Anomalous? *Physical Review Letters*. 1995;75(21):3874-3877.
- Fecht HJ. Thermodynamic properties and stability of grain boundaries in metals based on the universal equation of state at negative pressure. *Acta Metallurgica et Materialia*. 1990;38(10):1927-1932.

20. de Lima JC, dos Santos VHF, Grandi TA, D'Ajello PCT, Dmitriev A. Thermodynamic considerations about the formation of alloys by mechanical alloying. *Physical Review B*. 2000;62(13):8871-8877.
21. Prates PB, Maliska AM, Ferreira AS, Poffo CM, Borges ZV, de Lima JC, et al. Structural, thermal, and photoacoustic study of nanocrystalline Cr₃Ge produced by mechanical alloying. *Journal of Applied Physics*. 2015;118(15):154903.
22. FIZ. *Inorganic Crystal Structure Database (ICSD)*. Karlsruhe: Gmelin—Institute für Anorganische Chemie and Fachinformationszentrum (FIZ); 1995.
23. Rietveld HM. A profile refinement method for nuclear and magnetic structures. *Journal of Applied Crystallography*. 1969;2:65-71.
24. Larson AC, von Dreele RB. *General Structure Analysis System (GSAS)*. Report LAUR 86-748. Los Alamos: Los Alamos National Laboratory; 2000.
25. de Lima JC, Cella NL, Miranda LCM, An Chying C, Franzan AH, Leite NF. Photoacoustic characterization of chalcogenide glasses: Thermal diffusivity of Ge_xTe_{1-x}. *Physical Review B*. 1992;46:14186-14189.
26. Young RA, ed. *The Rietveld Method*. Oxford: Oxford University Press; 1996.
27. Rodriguez-Carvajal J. Study of micro-structural effects by powder diffraction using the program FULLPROF. Available from: <http://www.cdifx.univ-rennes1.fr/fps/Microstructural_effects.pdf>. Access in 27/05/2017.
28. Dasgupta P. On the intrinsic hook effect associated with pseudo-Voigt profiles. *Journal of Applied Crystallography*. 2002;35(Pt 2):267-269.
29. Poffo CM, de Lima JC, Souza SM, Triches DM, Grandi TA, de Biasi RS. Structural, thermal and optical study of nanocrystalline silicon produced by ball milling. *Journal of Raman Spectroscopy*. 2010;41(12):1606-1609.
30. Wagner CNJ. Diffraction analysis of liquid metals and alloys. In: Beer SZ, ed. *Liquid Metals: Chemistry and Physics*. New York: Marcel Dekker; 1972.
31. Maret M, Chieux P, Hicter P, Atzmon M, Johnson WL. Partial structure factors and chemical short-range order in Ni₃₃Y₆₇ and Cu₃₃Y₆₇ metallic glasses. *Journal of Physics F: Metal Physics*. 1987;17(2):315.
32. Atomic Softek. *Crystal Office 98 software*. Hamilton: Atomic Softek.
33. Mangin P. *Les Amorphes Métalliques*. Paris: Les Editions de Physique; 1984.
34. Rosencwaig A, Gersho A. Theory of the photoacoustic effect with solids. *Journal of Applied Physics*. 1976;47(1):64.
35. Vargas H, Miranda LCM. Photoacoustic and related photothermal techniques. *Physics Reports: A Review Section of Physics Letters*. 1988;161(2):43-101.
36. Pinto Neto A, Vargas H, Leite NF, Miranda LCM. Photoacoustic characterization of semiconductors: Transport properties and thermal diffusivity in GaAs and Si. *Physical Review B*. 1990;41(14):9971.
37. Souza SM, Trichês DM, de Lima JC, Grandi TA, de Biasi RS. Structural, optical and photoacoustic study of Sb₂Te₃ prepared by mechanical alloying. *Physica B: Condensed Matter*. 2010;405(13):2807-2814.
38. Poffo CM, de Lima JC, Souza SM, Trichês DM, Grandi TA, de Biasi RS. Photoacoustic study of nanocrystalline silicon produced by mechanical grinding. *Physica B: Condensed Matter*. 2011;406(8):1627-1632.
39. Trichês DM, Souza SM, de Lima JC, Grandi TA, Campos CEM. Structural and photoacoustic studies of Zn₄Sb₃ and ZnSb phases prepared by mechanical alloying. *Journal of Applied Physics*. 2009;105(6):063518.
40. de Lima JC, Schmitt M, de Souza SM, Almeida TO, Jerônimo AR, Trichês DM, et al. Structural and thermal study of nanostructured GaSb alloy prepared by mechanical alloying. *Journal of Alloys and Compounds*. 2007;436(1-2):13-18.
41. Caillat T, Fleurial JP, Borshchevsky A. Growth and some properties of Cr₁₁Ge₁₉. *Journal of Alloys and Compounds*. 1997;252(1-2):12-15.
42. Lichtenecker K. Die Dielektrizitätskonstante künstlicher und natürlicher Mischkörper. *Physikalische Zeitschrift*. 1926;27:115-118.
43. Simpkin R. Derivation of Lichtenecker's Logarithmic Mixture Formula From Maxwell's Equations. *IEEE Transactions on Microwave Theory and Techniques*. 2010;58(3):545-550.
44. ChemGlobe. *Germanium*. Available from: <http://chemglobe.org/ptoe/_32.php>. Access in: 27/05/2017.
45. Ur SC, Nash P, Kim IH. Mechanical alloying and thermoelectric properties of Zn₄Sb₃. *Journal of Materials Science*. 2003;38(17):3553-3558.